



A Hint of a Low-energy Excess in Cosmic-Ray Fluorine

M. J. Boschini^{1,2}, S. Della Torre¹, M. Gervasi^{1,3}, D. Grandi^{1,3}, G. Jóhannesson^{4,5}, G. La Vacca^{1,3}, N. Masi^{6,7}, I. V. Moskalenko^{8,9}, S. Pensotti^{1,3}, T. A. Porter^{8,9}, L. Quadrani^{6,7}, P. G. Rancoita¹, D. Rozza¹, and M. Tacconi^{1,3}

¹ INFN, Milano-Bicocca, Milano, Italy

² CINECA, Segrate, Milano, Italy

³ Physics Department, University of Milano-Bicocca, Milano, Italy

⁴ Science Institute, University of Iceland, Dunhaga 3, IS-107 Reykjavik, Iceland

⁵ NORDITA, Roslagstullsbacken 23, 106 91 Stockholm, Sweden

⁶ INFN, Bologna, Italy

⁷ Physics Department, University of Bologna, Bologna, Italy

⁸ Hansen Experimental Physics Laboratory, Stanford University, Stanford, CA 94305, USA

⁹ Kavli Institute for Particle Astrophysics and Cosmology, Stanford University, Stanford, CA 94305, USA

Received 2021 June 3; revised 2021 October 2; accepted 2021 October 11; published 2022 January 31

Abstract

Since its launch, the Alpha Magnetic Spectrometer–02 (AMS-02) has delivered outstanding quality measurements of the spectra of cosmic-ray (CR) species (\bar{p} , e^\pm) and nuclei (H–O, Ne, Mg, Si, Fe), which resulted in a number of breakthroughs. The most recent AMS-02 result is the measurement of the spectrum of CR fluorine up to ~ 2 TV. Given its very low solar system abundance, fluorine in CRs is thought to be mostly secondary, produced in fragmentations of heavier species, predominantly Ne, Mg, and Si. Similar to the best-measured secondary-to-primary boron to carbon nuclei ratio that is widely used to study the origin and propagation of CR species, the precise fluorine data would allow the origin of Si-group nuclei to be studied independently. Meanwhile, the secondary origin of CR fluorine has never been tested in a wide energy range due to the lack of accurate CR data. In this paper, we use the first ever precise measurements of the fluorine spectrum by AMS-02 together with ACE-CRIS and Voyager 1 data to actually test this paradigm. Our detailed modeling shows an excess below 10 GV in the fluorine spectrum that may hint at a primary fluorine component. We also provide an updated local interstellar spectrum (LIS) of fluorine in the rigidity range from a few MV to ~ 2 TV. Our calculations employ the self-consistent GALPROP–HELMOD framework that has proved to be a reliable tool in deriving the LIS of CR \bar{p} and e^- , and nuclei $Z \leq 28$.

Unified Astronomy Thesaurus concepts: Secondary cosmic rays (1438); Heliosphere (711); Galaxy abundances (574); Interstellar medium (847); Galactic cosmic rays (567); Interplanetary medium (825)

Supporting material: machine-readable tables

1. Introduction

The precise data delivered by the new generation of space instrumentation allow stellar nucleosynthesis, properties of the interstellar medium (ISM), and the origin of cosmic rays (CRs) to be probed to a much finer detail than was possible just a decade ago. The measurements provided by individual spacecraft can be combined to cover the enormous range of rigidities, from a few MV to tens of TV, where the individual spectra of CR species are shaped by many different processes. Their analysis and interpretation enables the discoveries of new phenomena far outside of the local solar neighborhood.

The spectrum of CR fluorine from AMS-02 (Aguilar et al. 2021a) is the latest¹⁰ in a series of publications of spectra of the most abundant species, H–O, Ne, Mg, Si, and Fe (Aguilar et al. 2014, 2015a, 2015b, 2016a, 2016b, 2017, 2018a, 2018b, 2019a, 2019b, 2020, 2021c). Fluorine is less studied because its CR abundance is 100 and 10 times lower than that of its neighbors, oxygen and neon, correspondingly. Previous measurement of its spectrum in the range 0.62–35 GeV

nucleon⁻¹ was made by the HEAO-3-C2 instrument in 1979–1981 (Engelmann et al. 1990). Although it was an excellent instrument for its epoch, HEAO-3-C2 measurements exhibit significant systematic uncertainties when compared to the AMS-02 data (see detailed analyses in Boschini et al. 2020a, 2021).

The secondary-to-primary nuclei ratio in CRs is widely used in astrophysics to derive the parameters of Galactic CR propagation for an assumed model phenomenology. The derived parameters are then applied to all CR species from electrons and antiprotons, all the way up to the Fe-group nuclei. The best-measured B/C ratio is used most often. Other nuclei that are rare in the solar system, such as Li, Be, F, Sc, and V, are thought to be almost entirely produced by the fragmentation of heavier CR species. Their precise measurements can be used to probe the origin and propagation of specific groups of nuclei: the B/C ratio for the C–N–O group, F/Si for the Si group, and (Sc+V)/Fe for the Fe group. However, this common wisdom has never been tested in a wide energy range due to the lack of accurate data. The first ever precisely measured fluorine spectrum by AMS-02 (Aguilar et al. 2021a) together with ACE-CRIS (Lave et al. 2013) and Voyager 1 (Cummings et al. 2016) data offer a possibility to actually test this paradigm.

In this paper we analyze the new CR fluorine data and test their consistency with measurements of other species. We show that the spectrum of fluorine exhibits an excess below 10 GV and argue that it could be a signature of a primary fluorine component. We

¹⁰ Spectra of Na and Al have just been published (Aguilar et al. 2021b).



also provide an updated local interstellar spectrum (LIS) of fluorine in the rigidity range from a few MV to ~ 2 TV. Our calculations and interpretation employ the GALPROP¹¹–HELMOD¹² framework that is proved to be a reliable tool in deriving the LIS of CR species (Boschini et al. 2019, 2020a).

This is the third in a series of papers in which the detailed analysis of precise AMS-02 measurements taken together with Voyager 1 and ACE-CRIS data yields unexpected excesses in the spectra of CR species. The first two were evidence of the primary lithium in CRs (Boschini et al. 2020b), and a discovery of the low-energy excess in iron (Boschini et al. 2021).

2. Calculations

In this work we are using the same CR propagation model with distributed reacceleration and convection that was used in our previous analyses (for more details, see Boschini et al. 2017, 2018a, 2018b, 2020a, 2020b, 2021). The latest version of the GALPROP code for Galactic propagation of CRs is described in detail in a recent paper by Boschini et al. (2020a); see also references therein.

Full details of the latest HELMOD code version 4 for heliospheric propagation are provided in Boschini et al. (2019). It solves the Fokker–Planck equation for heliospheric propagation in a Kolmogorov formulation backward in time (Bobik et al. 2016). The accuracy of the solution was tested using the Crank–Nicholson technique and found to be better than 0.5% at low rigidities. The large number of simulated events ensures that the statistical errors are negligible compared to the other modeling uncertainties.

When comparing our calculations with data collected over an extended period of time (AMS-02), variations in the solar activity are addressed in the following way. The propagation equation is solved for each Carrington rotation, and the numerical results are then combined according to the AMS-02 exposure and the time period. This approach is equivalent to application of a weighted average that accounts for both the exposure time and absolute counting rate variations.

The values of propagation parameters in the ISM along with their confidence limits are derived from the best available CR data using the Markov Chain Monte Carlo routine. Here, we use the same method as described in Boschini et al. (2017). Five main propagation parameters that affect the overall shape of CR spectra were left free in the scan using GALPROP running in 2D mode: the Galactic halo half-width z_h , the normalization of the diffusion coefficient D_0 at the reference rigidity $R = 4$ GV and the index of its rigidity dependence δ , the Alfvén velocity V_{Alf} , and the gradient of the convection velocity dV_{conv}/dz ($V_{\text{conv}} = 0$ in the plane, $z = 0$). Their best-fit values tuned to the AMS-02 data are listed in Table 1 and are the same as those obtained in Boschini et al. (2020a). The radial size of the Galaxy does not significantly affect the values of propagation parameters and was set to 20 kpc. We also introduced a factor β^η in the diffusion coefficient, where $\beta = v/c$, and η was left free. The best-fit value of $\eta = 0.70$ improves the agreement at low energies, and slightly affects the choice of injection indices γ_0 and γ_1 . A detailed discussion of the injection (I) and propagation (P) scenarios of the 350 GV break can be found in the papers by Vladimirov et al. (2012) and Boschini et al. (2020a).

Table 1
Best-fit Propagation Parameters for I and P Scenarios

Parameter	Units	Best Value	Error
z_h	kpc	4.0	0.6
$D_0(R = 4 \text{ GV})$	$\text{cm}^2 \text{ s}^{-1}$	4.3×10^{28}	0.7
δ^a		0.415	0.025
V_{Alf}	km s^{-1}	30	3
dV_{conv}/dz	$\text{km s}^{-1} \text{ kpc}^{-1}$	9.8	0.8

Note.

^a The P scenario assumes a break in the diffusion coefficient with index $\delta_1 = \delta$ below the break and index $\delta_2 = 0.15 \pm 0.03$ above the break at $R = 370 \pm 25$ GV (for details see Boschini et al. 2020b).

The corresponding B/C ratio also remains the same (see Figure 4 of Boschini et al. 2020a), and compares well with all available measurements: Voyager 1 (Cummings et al. 2016), ACE-CRIS¹³ (Lave et al. 2013), AMS-02 (Aguilar et al. 2018a), ATIC-2 (Panov et al. 2009), CREAM (Ahn et al. 2008, 2009), and NUCLEON (Grebnyuk et al. 2019).

3. Results and Discussion

Figure 1 (top-left panel) shows a comparison of the AMS-02 fluorine data (Aguilar et al. 2021a) with the calculated spectrum assuming the species is entirely secondary. The calculated spectral shape resembles the data, while the default normalization appears to be a bit too high over the whole range. The top-right panel shows the default fluorine spectrum multiplied by a factor of 0.896 and the corresponding residuals. Here, we normalized our calculated spectrum to the data in the middle rigidity range 10–100 GV. We attribute this $\sim 10\%$ discrepancy to the errors in the isotopic production cross sections that are well within their typical uncertainties (see a detailed discussion in Appendix C.1 in Boschini et al. 2020a). The quality of the fit improves with this modification. But, after the renormalization, there is now a $\sim 6\%$ – 7% excess below ~ 10 GV. At higher rigidities > 100 GV, the residuals become larger, as do the error bars, which keep the overall agreement to better than 1σ .

The bottom panel in Figure 1 shows the renormalized fluorine ($\times 0.896$) with the primary propagated fluorine component, where the total calculated spectrum is tuned to the data. The dashed cyan line shows separately the propagated primary fluorine component. An addition of the primary fluorine removes the excess below 10 GV and preserves the good agreement with data above ~ 10 GV. The parameters of the injection spectrum of primary fluorine are summarized in Table 2. The injection spectrum is steep with index 2.90 above 4.50 GV (Figure 2) implying that it might be accelerated in a weak shock.

The rationale behind this spectral renormalization is simple. The effects of the nuclear structure are important below $\sim 1 \text{ GeV nucleon}^{-1}$; it is where the characteristic features in the reaction cross sections are typically observed. Above this energy the reaction cross sections are usually flat. The AMS-02 data in the heliosphere are taken above 2 GV or $\sim 1 \text{ GeV nucleon}^{-1}$, which corresponds to ~ 2.5 – 3 GV or ~ 1.25 – $1.5 \text{ GeV nucleon}^{-1}$ in the ISM. Therefore, the application of a single renormalization factor that takes into account possible errors in the isotopic production cross sections is well justified.

¹¹ Available from <http://galprop.stanford.edu>.

¹² <http://www.helmod.org/>

¹³ http://www.srl.caltech.edu/ACE/ASC/level2/cris_l2desc.html

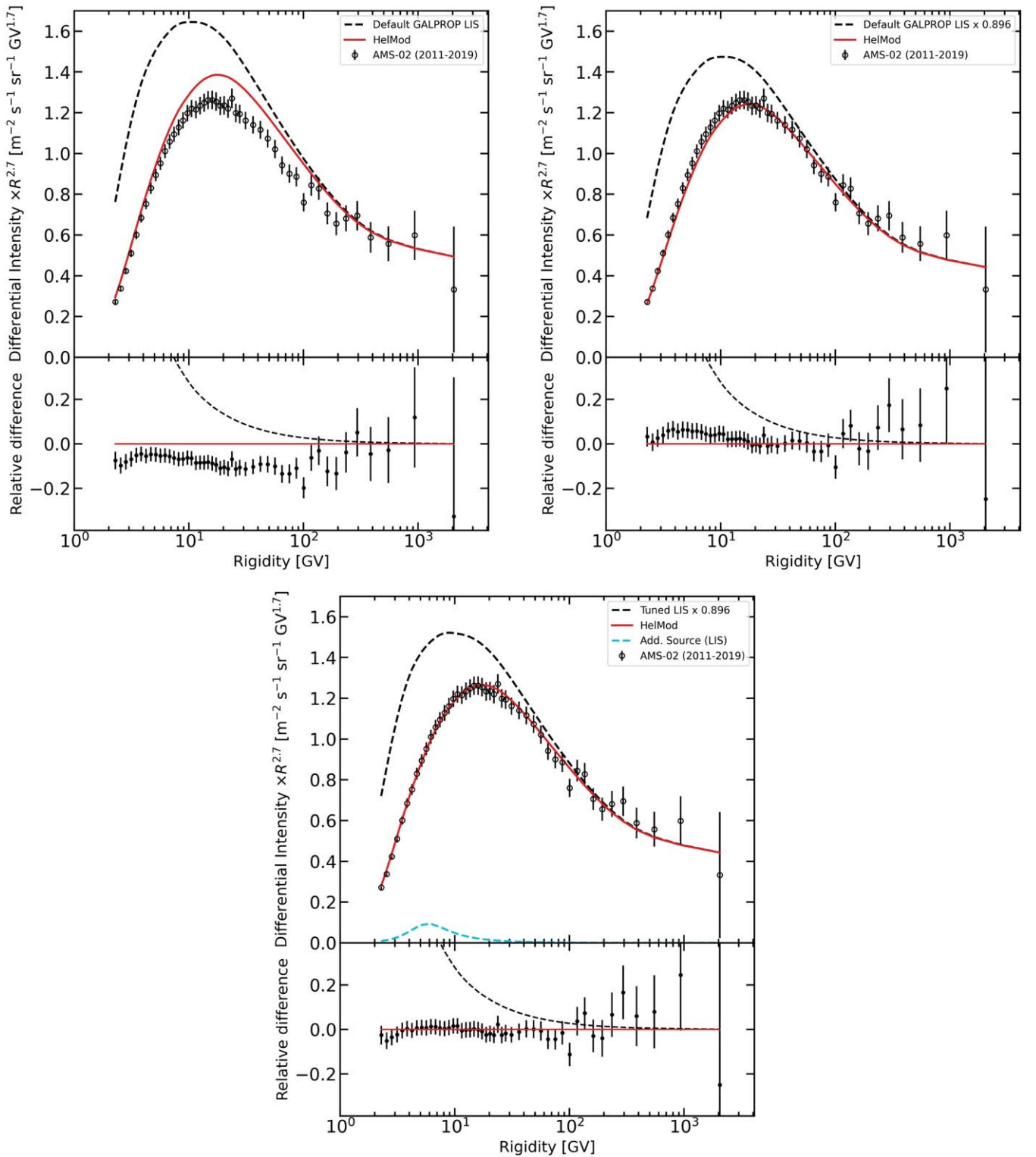


Figure 1. Top left: a comparison of the calculated default spectrum of secondary fluorine with the AMS-02 data (Aguilar et al. 2021a). Top right: the calculated default spectrum is multiplied by an energy-independent factor 0.896, as discussed in the text. Bottom: the same as in the top right, but with an added primary fluorine component (see the injection spectrum in Table 2), where the total calculated spectrum is tuned to the data. The dashed cyan line shows separately the propagated primary fluorine component. In all panels, the dashed gray line shows the LIS, and the solid red line is the corresponding modulated spectrum. Each panel also shows the relative difference between our calculations and the data set.

The calculated spectra of Ne, Mg, and Si, which are the main contributors to the production of secondary F, and the B/C ratio were tuned to the high-precision measurements by Voyager 1, ACE-CRIS, and AMS-02 (see Figures 3 and 4 in Boschini et al. 2020a). This eliminates possible systematic errors in the calculation of the

spectrum of secondary F due to the poorly constrained propagation parameters, especially in the rigidity range where the excess is observed. In Figures 3 and 4 the calculated F/Si and F/Ne ratios are compared with Voyager 1 (Cummings et al. 2016), ACE-CRIS (Lave et al. 2013), HEAO-3-C2 (Engelmann et al. 1990), and

Table 2
The Injection Spectrum of Primary Fluorine

Source	Abundance	Spectral parameters									
		γ_0	R_0 (GV)	s_0	γ_1	R_1 (GV)	s_1	γ_2	R_2 (GV)	s_2	γ_3
^{19}F	0.63	0.10	1.00	0.30	1.00	3.80	0.32	3.8	8.0	0.35	3.12

Note. See Equation (2) in Boschini et al. (2020a) for parameter definitions. Shown are $|s_i|$ values; note that s_i is negative/positive for $|\gamma_i| \leq |\gamma_{i+1}|$.

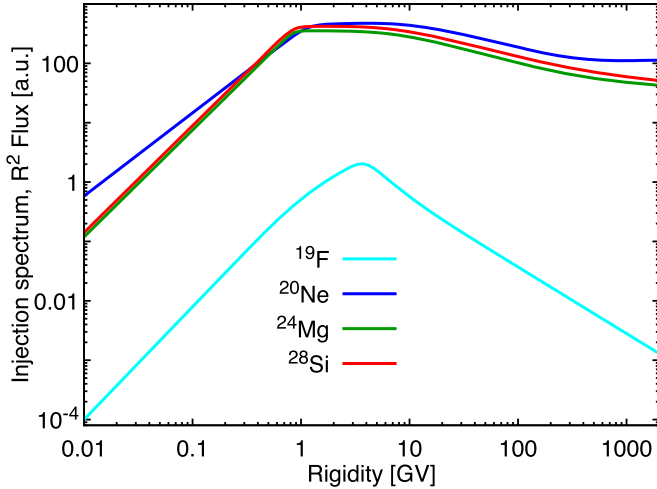


Figure 2. The injection spectra of primary ^{19}F and major progenitors of secondary ^{19}F : ^{20}Ne , ^{24}Mg , and ^{28}Si . The parameters for ^{19}F are given in Table 2, and for ^{20}Ne , ^{24}Mg , and ^{28}Si , are taken from Tables 2 and 3 in Boschini et al. (2020a).

AMS-02 data (Aguilar et al. 2020, 2021a). The top-left panels show the calculated default F/Si and F/Ne ratios with secondary fluorine only. The top-right panels show the default ratios with renormalized fluorine ($\times 0.896$). The renormalized plots exhibit the excess below 10 GV, while still agreeing with ACE-CRIS and Voyager 1 data. Above this rigidity the agreement with AMS-02 data is good. The bottom panels show the calculated F/Si and F/Ne ratios with the renormalized fluorine ($\times 0.896$) and with the primary propagated fluorine component tuned to the data (Figures 1, bottom panel). The dashed cyan line shows separately the propagated ratios with primary fluorine only. In all plots, the Voyager 1, ACE-CRIS, and HEAO-3-C2 data are converted from kinetic energy per nucleon to rigidity assuming $A/Z = 2$ for Si and Ne. In Figure 4, AMS-02 data are shown as the data points for the identical rigidity bins for F and Ne fluxes (< 30 GV) and are interpolated where the rigidity binning is different (> 30 GV). The shaded areas show the measured ratios with the width corresponding to the 1σ error.

Apart from the overall normalization, possibly attributable to insufficiently constrained fluorine production cross sections (which however become fairly flat $\gtrsim 1$ GeV nucleon $^{-1}$), we see three possible reasons for the observed low-energy (< 10 GV) excess: (1) an underestimate of the total inelastic cross section of fluorine, which has a broad minimum at a few 100 MeV nucleon $^{-1}$ (see, e.g., Figure 1 in Wellisch & Axen 1996), (2) the effective diffusion coefficient in the rigidity range 1–10 GV is somewhat smaller than that derived from the B/C ratio, and (3) a primary fluorine component. We note that the fine-tuning of the low-rigidity part in the Ne, Mg, and Si spectra does not help to remove the excess in fluorine entirely, though it could make it somewhat less significant. We, therefore, proceed with our original Ne, Mg, and Si spectra that are not fine-tuned to the fluorine data.

Underestimation of the total inelastic cross section of fluorine as a primary reason for the excess can be excluded by consideration of the accelerator data. Bobchenko et al. (1979) provide a table of measured proton-nucleus cross sections for the proton momenta from 5 GeV c^{-1} to 9 GeV c^{-1} that correspond to the ambient ^{19}F rigidity range 11–19 GV in the inverse kinematics, while the measurement accuracy is stated as 1%–2%. The average value of the total inelastic cross section in this interval is 350.9 mb; the deviations do not exceed ± 5 mb, with just two out of a total of seventeen points being clear outliers at 361 ± 5 mb and 358 ± 5 mb. This is the energy range where the total inelastic cross sections are flat and they are easier to measure than the isotopic production. Besides, the total fluorine fragmentation cross section can be easily scaled from the nearby oxygen and neon cross sections. The parameterizations of the total inelastic cross sections used in the calculations (e.g., Barashenkov & Polanski 1994) are tuned to the available data. Therefore, given a weak rigidity dependence of the diffusion coefficient, a possible error in the total inelastic cross section would be equivalent to a simple renormalization of the fluorine flux, very similar to the renormalization of the production cross sections. That makes a significant error at around 5 GV, the maximum in the fluorine excess, rather unlikely. We note the absence of a similar excess in the spectra of neighboring nuclei, such as O, Ne, Mg, and Si (Boschini et al. 2020a).

Variations in the diffusion coefficient seem unlikely as well. The ratio F/Si is the Si-group analog of the widely used B/C or B/O ratio for the light species. Both the F/Si and F/Ne ratios are consistent with predictions based on the propagation parameters derived from the B/C ratio above 10 GV. However, they demonstrate a $\approx 6\%$ – 7% deviation in the rigidity range 3–7 GV. In terms of the diffusion coefficient, it would mean that the effective diffusion coefficient in this rigidity range probed by the F/Si and F/Ne ratios is about 10% smaller than that in the case of the B/C ratio. Assuming the same distribution of sources of CR C, O, Ne, Mg, and Si nuclei, and given that the total inelastic cross sections of ^{16}O (320 mb) and ^{20}Ne (380 mb) are about the same, with neon being the main contributor to CR fluorine (see Figure 1 in Moskalenko et al. 2013 and Appendix C.1 in Boschini et al. 2020a), the B/C, F/Si, and F/Ne ratios are probing essentially the same Galactic volume. The total inelastic cross section of ^{28}Si (465 mb) is only a factor of ~ 1.3 larger, which corresponds to the effective propagation distance of a factor of ~ 0.90 smaller than that of O and Ne (Jóhannesson et al. 2016). Here, the values are given for the energy range of the excess, i.e., at a few GeV nucleon $^{-1}$.

Meanwhile, we note that the measured spectra of the light primary nuclei He, C, and O are flatter than the spectra of the Si-group nuclei, Ne, Mg, and Si, with the difference in indices being ~ 0.045 above 90 GV (Aguilar et al. 2020). If the difference in indices between O and Si nuclei is confirmed with larger statistics, it may indicate a somewhat different distribution of their sources. Besides that, measurements of other species, such as Na and Al spectra, the P/S ratio, and especially the ratio of the iron-group

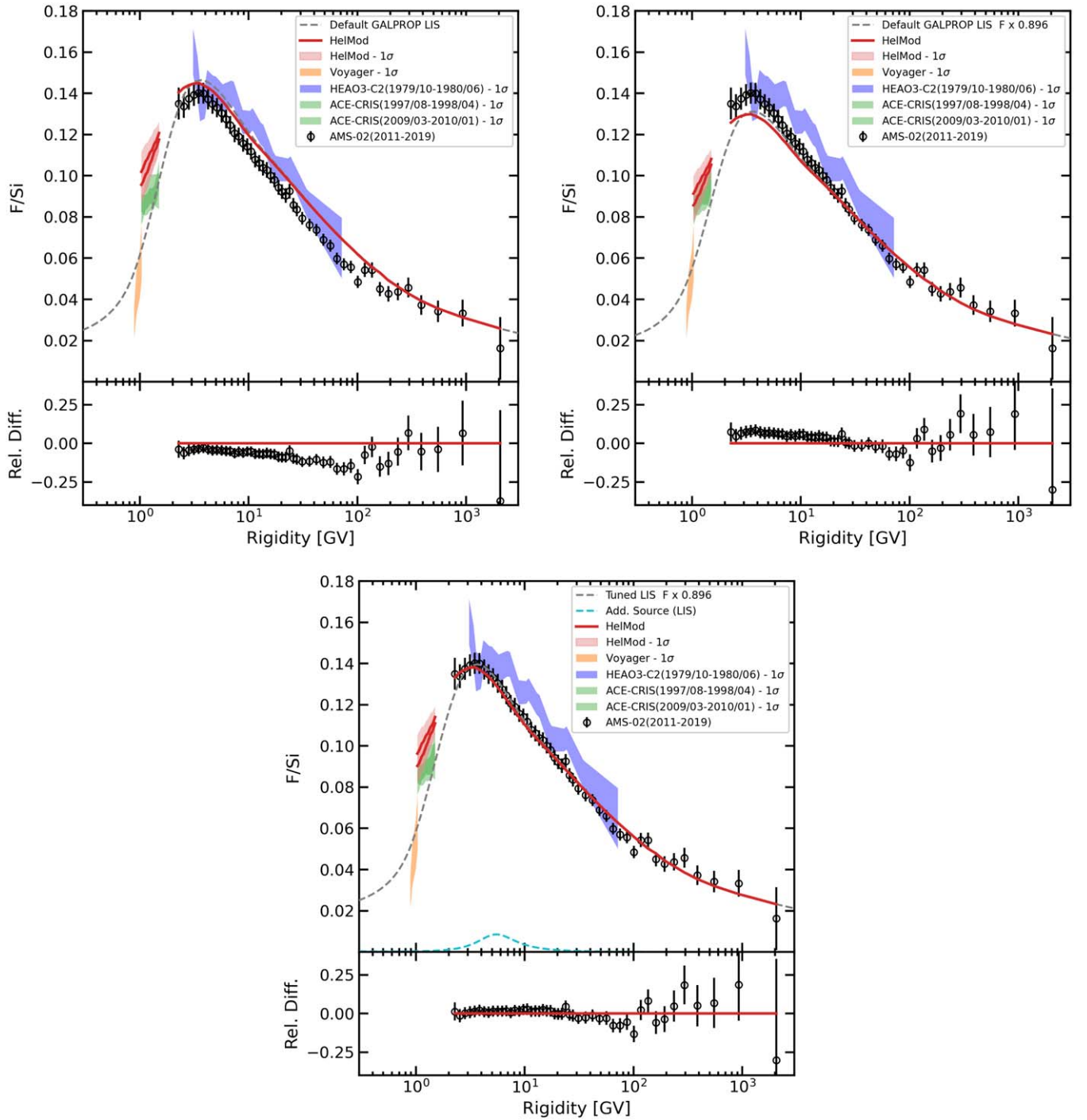


Figure 3. Top left: the calculated default F/Si ratio compared with Voyager 1 (Cummings et al. 2016), ACE-CRIS (Lave et al. 2013), HEAO-3-C2 (Engelmann et al. 1990), and AMS-02 data (Aguilar et al. 2020, 2021a). Top right: the calculated default F/Si ratio is renormalized with a factor of 0.896. Bottom: the same as in the top right, but with an added primary fluorine component (see the injection spectrum in Table 2), where the total calculated fluorine spectrum is tuned to the data (Figure 1). The dashed cyan line shows separately the propagated ratio with primary fluorine only. In all panels, the dashed gray line shows the LIS ratio, and the solid red line is the corresponding modulated ratio. In all plots, the Voyager 1, ACE-CRIS, and HEAO-3-C2 data are converted from kinetic energy per nucleon to rigidity assuming $A/Z = 2$ for Si. These data are shown as shaded areas with the width corresponding to the 1σ error. Each panel also shows the relative difference between our calculations and the AMS-02 data set.

nuclei $(Sc+V)/Fe$ can be used to probe the variations of the diffusion coefficient in the local Galaxy.

An interesting possibility would be the presence of primary fluorine at low energies. We already discussed a hint of primary fluorine in CRs in Boschini et al. (2020a, Appendix C.1), but the large error bars and large scattering of the HEAO-3-C2 data points made this result inconclusive. The first ever accurate measurement

of the fluorine spectrum in the rigidity range 2 GV–2 TV (Aguilar et al. 2021c) allows the fluorine spectrum to be analyzed in finer detail, and it seems that the excess also appears in the new data.

We do not discuss here the possibility of instrumental errors, as they are rather unlikely. The AMS-02 detector, with its multiple redundancies, provides state-of-the-art measurements of the CR species (Aguilar et al. 2021d). Before its launch, AMS-02 was

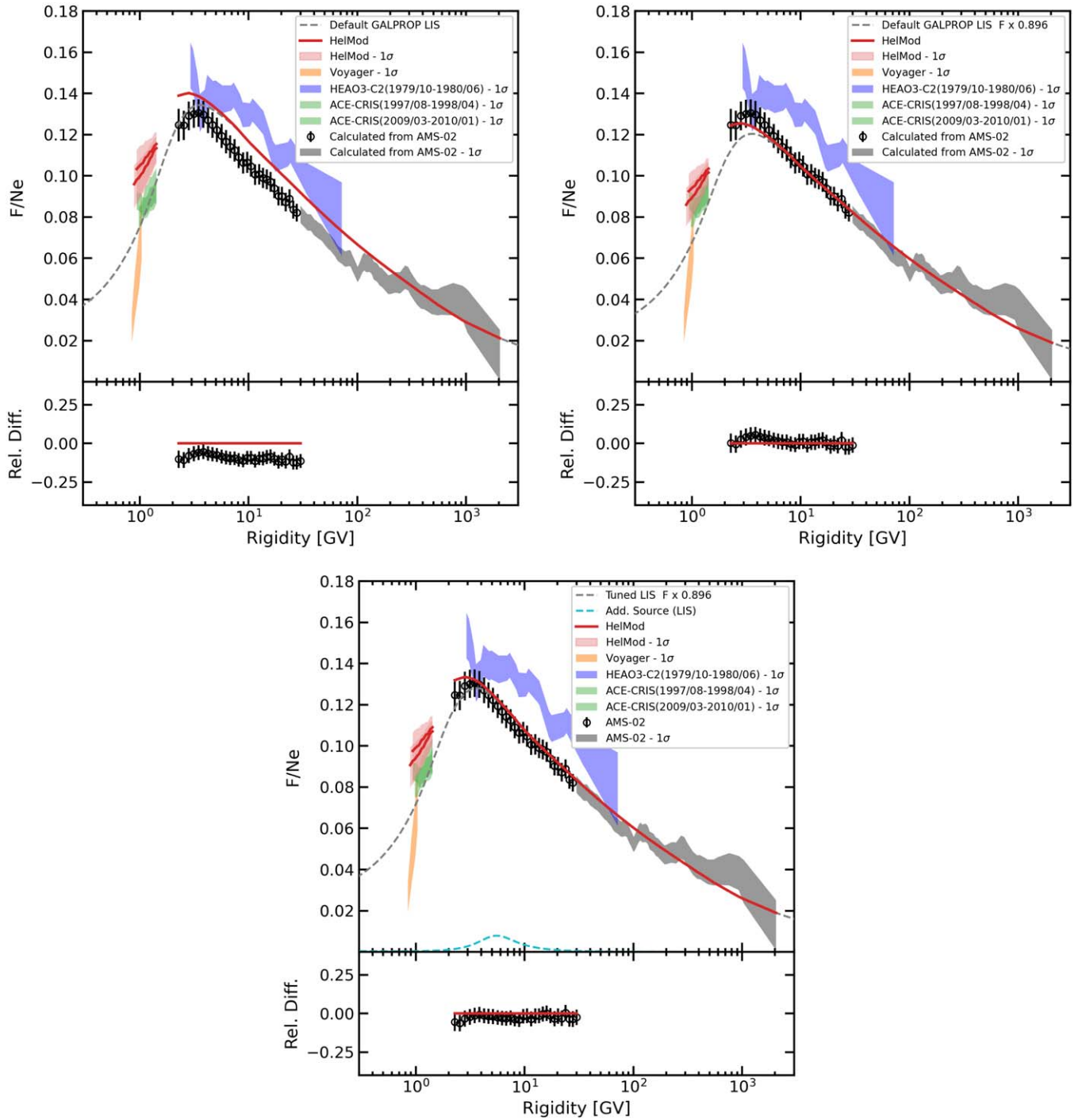


Figure 4. Top left: the calculated default F/Ne ratio as compared with Voyager 1 (Cummings et al. 2016), ACE-CRIS (Lave et al. 2013), HEAO-3-C2 (Engelmann et al. 1990), and AMS-02 data (Aguilar et al. 2020, 2021a). Top right: the calculated default F/Ne ratio is renormalized with a factor of 0.896. Bottom: the same as in the top right, but with an added primary fluorine component (see the injection spectrum in Table 2), where the total calculated fluorine spectrum is tuned to the data (Figure 1). The dashed cyan line shows separately the propagated ratio with primary fluorine only. In all panels, the dashed gray line shows the LIS ratio, and the solid red line is the corresponding modulated ratio. In all plots, the Voyager 1, ACE-CRIS, and HEAO-3-C2 data are converted from kinetic energy per nucleon to rigidity assuming $A/Z = 2$ for Ne. AMS-02 data are shown as the data points for the identical rigidity bins for F and Ne fluxes (<30 GV) and are interpolated where the rigidity binning is different (>30 GV). These data are shown as shaded areas with the width corresponding to the 1σ error. Each panel also shows the relative difference between our calculations and the AMS-02 data set, where the data points are available.

tested extensively at the CERN test beam with electrons, positrons, protons, and pions. During more than 10 yr of AMS-02 construction, a large international group of physicists have developed a comprehensive Monte Carlo simulation program for AMS-02. Importantly, the fragmentation cross sections of CR species inside the instrument are measured by AMS-02 itself using the silicon tracker layers. The procedure and survival probabilities

for different elements are described in Aguilar et al. (2021d). The data analysis is performed in parallel by several groups, which employ different methods. A good agreement between their results is required before a paper is submitted for publication.

In the Appendix, we provide an analytical parameterization of the secondary-only renormalized fluorine LIS, Equation (A1), and the total fluorine LIS, Equation (A2), that includes also the

primary component. The parameters are provided in Tables 3 and 4, respectively. We also provide numerical tables for both cases, which tabulate the LIS in rigidity R (Table 5) and in kinetic energy E_{kin} per nucleon (Table 6) for the secondary-only fluorine LIS, and corresponding Tables 7, 8 for the total fluorine LIS. The analytical parameterizations, Equations (A1) and (A2), and numerical tables include a rigidity-independent normalization factor, $a = 0.896$.

4. Primary Fluorine

Precise CR measurements over the last decade have led to the discoveries of new features in spectra of CR species, various breaks and excesses in the energy range from sub-GeV to multi-TeV. Using combined measurements of AMS-02, Voyager 1, and ACE-CRIS, we were able to establish the presence of primary lithium in CRs (Boschini et al. 2020b), and to discover the low-energy excess in iron (Boschini et al. 2021). In the present paper, we argue that the fluorine spectrum may also exhibit a low-energy excess. These excesses may harbor the keys to understanding our local Galactic environment. Here, we discuss potential sources of primary CR fluorine.

The ISM abundance of fluorine is anomalously low because it is easily destroyed in stars through either p - or α -captures. Its solar system abundance relative to oxygen ranges from $(\text{F}/\text{O})_{\odot} = 0.74 \times 10^{-4}$ in the solar photosphere to 1.05×10^{-4} in meteorites (Asplund et al. 2009). This can be compared with the derived F/O ratio in CR sources: $(\text{F}/\text{O})_{\text{srs}} = 4 \times 10^{-4}$ or $[\text{F}/\text{O}]_{\text{srs}} = 0.6\text{--}0.7$ dex depending on the $(\text{F}/\text{O})_{\odot}$ used, where $[\text{X}/\text{Y}] = \log_{10}(\text{X}/\text{Y}) - \log_{10}(\text{X}/\text{Y})_{\odot}$. Here, we integrated over the injection spectra of primary fluorine (Table 2) and oxygen (Tables 2 and 3 in Boschini et al. 2020a) above 1 GV, where the excess is observed. If integrated above 0.1 GV, then the ratio becomes $(\text{F}/\text{O})_{\text{srs}} = 1.7 \times 10^{-4}$ or $[\text{F}/\text{O}]_{\text{srs}} = 0.21\text{--}0.36$ dex, closer to the solar system abundance.

The origin of cosmic fluorine is still not well constrained. Several nucleosynthetic channels at different phases of stellar evolution have been suggested, but these must be constrained by observations. The main astrophysical sources of fluorine are thought to be supernovae Type II (SN II), Wolf-Rayet (WR) stars, and the asymptotic giant branch (AGB) of intermediate-mass stars (e.g., Meynet & Arnould 2000; Renda et al. 2004; Olive & Vangioni 2019). These sources become important at different stages of chemical evolution of the Galaxy, with the ν -spallation of neon in SN II dominating at early times in low-metallicity environments, while WR and AGB stars dominate at later stages at solar and supersolar metallicities. The calculations show that reaching the solar level of $[\text{F}/\text{O}] = 0$ at the present epoch requires all three types of sources to contribute (Renda et al. 2004).

Meanwhile, determining the fluorine abundance in stars is challenging. A diagnostic is via observations of molecular HF emission lines in the K and N bands ($2.1\text{--}2.4 \mu\text{m}$ and $8\text{--}13 \mu\text{m}$, respectively), which are observable only in cool giants ($T_{\text{eff}} < 4500$ K). Analysis of the spectra of K giants shows that the fluorine-to-oxygen abundance ratio $[\text{F}/\text{O}]$ increases as a function of oxygen abundance $[\text{O}/\text{H}]$ with a slope 1 ± 0.2 , and can reach $[\text{F}/\text{O}] \approx 0.4$ dex for $[\text{O}/\text{H}] \approx 0.2$ dex (Ryde et al. 2020). Behavior like this is typical of the so-called “secondary” elements, whose synthesis in stars involves nuclides pre-existing in the ISM gas of which stars form. A corresponding abundance ratio for the so-called “primary” elements would be a constant, because the abundances of primary elements increase proportionally to metallicity. An example of a primary element is oxygen.

The key isotope that contributes to the production of fluorine in different environments is ^{14}N , which is converted to fluorine via a series of proton and α captures $^{14}\text{N}(\alpha, \gamma)^{18}\text{F}$ (β^+) $^{18}\text{O}(p, \alpha)^{15}\text{N}(\alpha, \gamma)^{19}\text{F}$ in the presence of ^{13}C ; the latter is needed for the generation of protons (Goriely et al. 1990; Prantzos et al. 2018). Such reactions can take place in rapidly rotating massive stars, thermally pulsating AGB stars, and massive WR stars. Novae are also proposed as a possible source of fluorine through proton captures by ^{17}O . A useful review of fluorine nucleosynthesis is given in Ryde et al. (2020).

A possible identification of a primary CR fluorine component would provide another (indirect) way of studying the synthesis of this species in CR sources. If true, the fluorine overabundance in the CR sources ($[\text{F}/\text{O}]_{\text{srs}} = 0.6\text{--}0.7$ dex above 1 GV or $0.21\text{--}0.36$ dex above 0.1 GV) could hint at perhaps yet unknown processes acting at certain stages of stellar evolution. Important clues to the origin of primary fluorine, and the nature of CR sources in the local Galaxy, can be deduced from the observation (or non-observation) of low-energy excesses in the spectra of other mostly secondary elements of the Si group, such as Na and Al.

5. Conclusion

Using the combined data of AMS-02 (Aguilar et al. 2021c), ACE-CRIS (Lave et al. 2013), and Voyager 1 (Cummings et al. 2016) we analyzed the spectrum of fluorine over a wide rigidity range from MV to 2 TV. We found moderate discrepancies with the predictions made with the GALPROP-HELMOD framework.

First, the default normalization of the whole spectrum was found to be off by $\sim 10\%$. We attribute this discrepancy to the errors in the isotopic production cross sections that are well inside of their typical uncertainties. Second, the renormalized fluorine spectrum and renormalized F/Si and F/Ne ratios show an excess below 10 GV. We discuss possible origins of this excess and rule out the underestimate of the total inelastic cross section of fluorine and the variations in the diffusion coefficient as the primary reasons for the excess.

We conclude that a contribution of primary fluorine could not be ruled out at this point, but its confirmation requires more data. We present the derived injection spectrum of primary fluorine and discuss its main astrophysical sources. As in all our previous papers, we also provide an analytical parameterization and numerical tables of the fluorine LIS.

We are grateful to the anonymous referee for their thorough reading of the manuscript and useful remarks. Special thanks to Pavol Bobik, Giuliano Boella, Marian Putis, and Mario Zannoni for their continuous support of the HELMOD project and many useful suggestions. This work was carried out using the HELMOD tool, which is currently supported within ASIF-ASI (Agenzia Spaziale Italiana) Supported Irradiation Facilities – framework for space radiation environment activities, e.g., ASIF implementation agreements 2017-22-HD.0 ASI-ENEA, 2017-15-HD.0 ASI-INFN and ASIF implementation agreement involving ASI and Milano-Bicocca University. This work is also supported by ASI contract ASI-INFN I/002/13/0 and ESA (European Space Agency) contract 4000116146/16/NL/HK. I.V.M. and T.A.P. acknowledge support from NASA grant No. NNX17AB48G. This research has made use of the SSCD Cosmic rays database (Di Felice et al. 2017) and LPSC Database of Charged Cosmic Rays (Maurin et al. 2014).

Appendix

Analytical Parameterization and Numerical Tables of the Fluorine LIS

Here, we provide an analytical parameterization of the secondary-only renormalized fluorine LIS:

$$F_{\text{sec}}(R) = a \times \begin{cases} b + cR + dR^5 - fR^2 - gG(R)\sqrt{R} - hR^2G(R) - iRG^2(R), & R \leq 2.5 \text{ GV}, \\ R^{-2.7} \left[-\frac{l}{R} + mR^2 + \frac{n}{o+R} + \frac{p}{q+rR} + \frac{s}{R \tanh[o/(t+R)]} - u - vR \right], & R > 2.5 \text{ GV}, \end{cases} \quad (\text{A1})$$

where R is the particle rigidity in GV, the values of the fitting parameters from a to z are given in Table 3, and the function $G(x)$ is defined as:

$$G(x) = e^{-x^2}.$$

The analytical representation, Equation (A1), is also complemented by numerical tables calculated for the I scenario, which tabulate the LIS in rigidity R (Table 5) and in kinetic energy E_{kin} per nucleon (Table 6).

We also provide an analytical parameterization of the total fluorine LIS, which includes the primary component:

$$F_{\text{tot}}(R) = a \times \begin{cases} o - pR - qR \log R - rG(R) + sG^3(R) + tR^2G(R) - uG[v + zG(R)], & R \leq 2.5 \text{ GV}, \\ R^{-2.7} \left[b + cR + dR^2 - f\sqrt{R} - gR\sqrt{R} - \frac{h}{R} - \frac{i}{\sqrt{R}} + \frac{l}{m+R} + \frac{n}{R+\sqrt{R}} \right], & R > 2.5 \text{ GV}, \end{cases} \quad (\text{A2})$$

where R is the particle rigidity in GV, the values of the fitting parameters from a to z are given in Table 4, and the function $G(x)$ is defined above. The analytical representation, Equation (A2), is also complemented by numerical tables calculated for the I scenario, which tabulate the LIS in rigidity R (Table 7) and in kinetic energy E_{kin} per nucleon (Table 8).

Table 3
Parameters of the Fit to the Secondary-only Renormalized Fluorine LIS, Equation (A1)

Param	Value	Param	Value	Param	Value	Param	Value
a	0.896e+0	g	2.2707e-2	n	1.1615e+2	s	6.2037e+1
b	3.0304e-3	h	2.6461e-2	o	2.1291e+1	t	5.2771e+0
c	1.4857e-1	i	9.9310e-2	p	2.7873e+1	u	2.5986e+0
d	4.7068e-4	l	6.6451e+1	q	1.7222e+2	v	2.0513e-7
f	5.5235e-2	m	2.0120e-13	r	1.0152e-2

Table 4
Parameters of the Fit to the Total Fluorine LIS, Equation (A2)

Param	Value	Param	Value	Param	Value	Param	Value
a	0.896e+0	g	1.16195e-8	n	2.57541e+1	s	4.77105e-2
b	6.12968e-1	h	1.37360e+1	o	1.81461e-1	t	9.94025e-3
c	7.19610e-6	i	4.02914e+0	p	2.45030e-2	u	2.03517e-2
d	7.17705e-12	l	1.01968e+2	q	9.31457e-3	v	1.58760e-1
f	2.22764e-3	m	4.69709e+1	r	2.29360e-1	z	1.98665e+0

Table 5
 $Z = 9$ —Secondary-only Renormalized Fluorine LIS

Rigidity GV	Differential Intensity								
9.114e−02	1.554e−04	7.359e−01	3.419e−02	1.018e+01	2.802e−03	5.322e+02	2.265e−08	3.346e+04	1.991e−13
9.565e−02	1.781e−04	7.735e−01	3.778e−02	1.105e+01	2.249e−03	5.858e+02	1.720e−08	3.684e+04	1.517e−13
1.004e−01	2.023e−04	8.132e−01	4.157e−02	1.200e+01	1.798e−03	6.449e+02	1.307e−08	4.057e+04	1.156e−13
1.053e−01	2.299e−04	8.551e−01	4.554e−02	1.304e+01	1.432e−03	7.100e+02	9.948e−09	4.467e+04	8.814e−14
1.105e−01	2.612e−04	8.992e−01	4.966e−02	1.419e+01	1.135e−03	7.816e+02	7.577e−09	4.919e+04	6.717e−14
1.160e−01	2.969e−04	9.459e−01	5.386e−02	1.545e+01	8.963e−04	8.605e+02	5.775e−09	5.417e+04	5.119e−14
1.217e−01	3.376e−04	9.952e−01	5.809e−02	1.684e+01	7.045e−04	9.474e+02	4.403e−09	5.965e+04	3.901e−14
1.277e−01	3.839e−04	1.047e+00	6.231e−02	1.836e+01	5.512e−04	1.043e+03	3.359e−09	6.569e+04	2.973e−14
1.341e−01	4.367e−04	1.103e+00	6.645e−02	2.004e+01	4.295e−04	1.148e+03	2.564e−09	7.233e+04	2.265e−14
1.407e−01	4.967e−04	1.161e+00	7.042e−02	2.189e+01	3.333e−04	1.264e+03	1.958e−09	7.965e+04	1.726e−14
1.476e−01	5.651e−04	1.223e+00	7.414e−02	2.392e+01	2.576e−04	1.392e+03	1.495e−09	8.771e+04	1.315e−14
1.549e−01	6.431e−04	1.289e+00	7.753e−02	2.616e+01	1.983e−04	1.533e+03	1.142e−09	9.658e+04	1.002e−14
1.626e−01	7.319e−04	1.358e+00	8.049e−02	2.862e+01	1.522e−04	1.688e+03	8.720e−10	1.064e+05	7.637e−15
1.707e−01	8.330e−04	1.432e+00	8.292e−02	3.133e+01	1.164e−04	1.858e+03	6.659e−10	1.171e+05	5.819e−15
1.791e−01	9.481e−04	1.511e+00	8.474e−02	3.431e+01	8.885e−05	2.046e+03	5.085e−10	1.290e+05	4.434e−15
1.880e−01	1.079e−03	1.595e+00	8.588e−02	3.759e+01	6.764e−05	2.253e+03	3.884e−10	1.420e+05	3.379e−15
1.973e−01	1.229e−03	1.684e+00	8.627e−02	4.121e+01	5.137e−05	2.481e+03	2.967e−10	1.564e+05	2.574e−15
2.070e−01	1.399e−03	1.780e+00	8.581e−02	4.518e+01	3.894e−05	2.731e+03	2.267e−10	1.722e+05	1.962e−15
2.173e−01	1.592e−03	1.881e+00	8.449e−02	4.957e+01	2.945e−05	3.008e+03	1.731e−10	1.896e+05	1.495e−15
2.280e−01	1.813e−03	1.990e+00	8.232e−02	5.439e+01	2.224e−05	3.312e+03	1.322e−10	2.088e+05	1.139e−15
2.393e−01	2.063e−03	2.107e+00	7.934e−02	5.970e+01	1.677e−05	3.647e+03	1.010e−10
2.512e−01	2.349e−03	2.232e+00	7.563e−02	6.555e+01	1.262e−05	4.015e+03	7.709e−11
2.637e−01	2.673e−03	2.366e+00	7.139e−02	7.199e+01	9.489e−06	4.421e+03	5.886e−11
2.767e−01	3.041e−03	2.511e+00	6.670e−02	7.908e+01	7.126e−06	4.869e+03	4.493e−11
2.905e−01	3.460e−03	2.666e+00	6.164e−02	8.688e+01	5.346e−06	5.361e+03	3.429e−11
3.049e−01	3.934e−03	2.833e+00	5.632e−02	9.548e+01	4.007e−06	5.903e+03	2.617e−11
3.201e−01	4.473e−03	3.014e+00	5.090e−02	1.049e+02	3.001e−06	6.501e+03	1.997e−11
3.360e−01	5.083e−03	3.210e+00	4.555e−02	1.154e+02	2.245e−06	7.158e+03	1.524e−11
3.527e−01	5.774e−03	3.421e+00	4.037e−02	1.268e+02	1.678e−06	7.882e+03	1.163e−11
3.702e−01	6.556e−03	3.650e+00	3.545e−02	1.395e+02	1.254e−06	8.679e+03	8.870e−12
3.887e−01	7.439e−03	3.899e+00	3.085e−02	1.534e+02	9.365e−07	9.558e+03	6.766e−12
4.081e−01	8.435e−03	4.169e+00	2.660e−02	1.687e+02	6.995e−07	1.052e+04	5.161e−12
4.285e−01	9.559e−03	4.463e+00	2.275e−02	1.856e+02	5.225e−07	1.159e+04	3.936e−12
4.499e−01	1.082e−02	4.783e+00	1.932e−02	2.042e+02	3.904e−07	1.276e+04	3.002e−12
4.724e−01	1.224e−02	5.132e+00	1.633e−02	2.247e+02	2.919e−07	1.405e+04	2.289e−12
4.961e−01	1.383e−02	5.513e+00	1.371e−02	2.472e+02	2.184e−07	1.547e+04	1.746e−12
5.210e−01	1.560e−02	5.929e+00	1.145e−02	2.720e+02	1.636e−07	1.704e+04	1.331e−12
5.472e−01	1.758e−02	6.384e+00	9.519e−03	2.993e+02	1.227e−07	1.876e+04	1.015e−12

Note. Differential Intensity units: $(\text{m}^2 \text{ s sr GV})^{-1}$.

(This table is available in machine-readable form.)

Table 6
 $Z = 9$ —Secondary—only Renormalized Fluorine LIS

E_{kin} GeV/n	Differential Intensity								
1.000e-03	7.085e-03	6.309e-02	2.059e-01	3.981e+00	6.024e-03	2.512e+02	4.782e-08	1.585e+04	4.203e-13
1.101e-03	7.739e-03	6.948e-02	2.179e-01	4.384e+00	4.822e-03	2.766e+02	3.631e-08	1.745e+04	3.203e-13
1.213e-03	8.378e-03	7.651e-02	2.296e-01	4.827e+00	3.847e-03	3.046e+02	2.760e-08	1.922e+04	2.441e-13
1.335e-03	9.073e-03	8.425e-02	2.411e-01	5.315e+00	3.057e-03	3.354e+02	2.100e-08	2.116e+04	1.861e-13
1.470e-03	9.826e-03	9.277e-02	2.521e-01	5.853e+00	2.420e-03	3.693e+02	1.600e-08	2.330e+04	1.418e-13
1.619e-03	1.065e-02	1.022e-01	2.623e-01	6.446e+00	1.907e-03	4.067e+02	1.219e-08	2.566e+04	1.081e-13
1.783e-03	1.154e-02	1.125e-01	2.716e-01	7.098e+00	1.497e-03	4.478e+02	9.296e-09	2.825e+04	8.235e-14
1.963e-03	1.250e-02	1.239e-01	2.798e-01	7.816e+00	1.170e-03	4.931e+02	7.091e-09	3.111e+04	6.275e-14
2.162e-03	1.355e-02	1.364e-01	2.868e-01	8.607e+00	9.110e-04	5.430e+02	5.413e-09	3.426e+04	4.782e-14
2.381e-03	1.469e-02	1.502e-01	2.924e-01	9.478e+00	7.065e-04	5.980e+02	4.133e-09	3.773e+04	3.644e-14
2.622e-03	1.594e-02	1.654e-01	2.964e-01	1.044e+01	5.457e-04	6.585e+02	3.156e-09	4.155e+04	2.777e-14
2.887e-03	1.728e-02	1.822e-01	2.986e-01	1.149e+01	4.199e-04	7.251e+02	2.411e-09	4.575e+04	2.116e-14
3.179e-03	1.875e-02	2.006e-01	2.990e-01	1.266e+01	3.221e-04	7.985e+02	1.841e-09	5.038e+04	1.612e-14
3.501e-03	2.034e-02	2.209e-01	2.973e-01	1.394e+01	2.463e-04	8.793e+02	1.406e-09	5.548e+04	1.228e-14
3.855e-03	2.207e-02	2.432e-01	2.936e-01	1.535e+01	1.879e-04	9.682e+02	1.073e-09	6.109e+04	9.361e-15
4.245e-03	2.395e-02	2.678e-01	2.878e-01	1.690e+01	1.430e-04	1.066e+03	8.200e-10	6.727e+04	7.133e-15
4.675e-03	2.599e-02	2.949e-01	2.800e-01	1.861e+01	1.086e-04	1.174e+03	6.264e-10	7.408e+04	5.435e-15
5.148e-03	2.820e-02	3.248e-01	2.700e-01	2.049e+01	8.228e-05	1.293e+03	4.785e-10	8.157e+04	4.141e-15
5.669e-03	3.061e-02	3.577e-01	2.580e-01	2.257e+01	6.223e-05	1.424e+03	3.655e-10	8.983e+04	3.155e-15
6.242e-03	3.322e-02	3.938e-01	2.443e-01	2.485e+01	4.698e-05	1.568e+03	2.791e-10	9.892e+04	2.404e-15
6.874e-03	3.606e-02	4.337e-01	2.291e-01	2.736e+01	3.541e-05	1.726e+03	2.132e-10
7.569e-03	3.913e-02	4.776e-01	2.128e-01	3.013e+01	2.666e-05	1.901e+03	1.628e-10
8.335e-03	4.246e-02	5.259e-01	1.960e-01	3.318e+01	2.004e-05	2.093e+03	1.243e-10
9.179e-03	4.607e-02	5.791e-01	1.789e-01	3.654e+01	1.505e-05	2.305e+03	9.485e-11
1.011e-02	4.998e-02	6.377e-01	1.617e-01	4.023e+01	1.129e-05	2.539e+03	7.240e-11
1.113e-02	5.421e-02	7.022e-01	1.447e-01	4.431e+01	8.461e-06	2.795e+03	5.525e-11
1.226e-02	5.878e-02	7.733e-01	1.283e-01	4.879e+01	6.336e-06	3.078e+03	4.216e-11
1.350e-02	6.372e-02	8.515e-01	1.128e-01	5.373e+01	4.739e-06	3.390e+03	3.217e-11
1.486e-02	6.905e-02	9.377e-01	9.830e-02	5.916e+01	3.543e-06	3.733e+03	2.455e-11
1.637e-02	7.480e-02	1.033e+00	8.501e-02	6.515e+01	2.647e-06	4.110e+03	1.873e-11
1.802e-02	8.099e-02	1.137e+00	7.293e-02	7.174e+01	1.977e-06	4.526e+03	1.428e-11
1.985e-02	8.764e-02	1.252e+00	6.209e-02	7.900e+01	1.477e-06	4.984e+03	1.090e-11
2.185e-02	9.479e-02	1.379e+00	5.249e-02	8.699e+01	1.103e-06	5.489e+03	8.310e-12
2.406e-02	1.024e-01	1.518e+00	4.411e-02	9.580e+01	8.243e-07	6.044e+03	6.337e-12
2.650e-02	1.106e-01	1.672e+00	3.691e-02	1.055e+02	6.162e-07	6.656e+03	4.833e-12
2.918e-02	1.194e-01	1.841e+00	3.073e-02	1.162e+02	4.610e-07	7.329e+03	3.685e-12
3.213e-02	1.286e-01	2.027e+00	2.547e-02	1.279e+02	3.453e-07	8.071e+03	2.810e-12
3.539e-02	1.384e-01	2.233e+00	2.103e-02	1.409e+02	2.590e-07	8.887e+03	2.142e-12

Note. Differential Intensity units: $(\text{m}^2 \text{ s sr GeV/n})^{-1}$.

(This table is available in machine-readable form.)

Table 7
 $Z = 9$ —Total Fluorine LIS with the Primary Component

Rigidity GV	Differential Intensity								
9.114e−02	1.774e−04	7.359e−01	3.673e−02	1.018e+01	2.886e−03	5.322e+02	2.275e−08	3.346e+04	1.991e−13
9.565e−02	2.032e−04	7.735e−01	4.051e−02	1.105e+01	2.312e−03	5.858e+02	1.727e−08	3.684e+04	1.518e−13
1.004e−01	2.306e−04	8.132e−01	4.449e−02	1.200e+01	1.845e−03	6.449e+02	1.312e−08	4.057e+04	1.157e−13
1.053e−01	2.619e−04	8.551e−01	4.866e−02	1.304e+01	1.467e−03	7.100e+02	9.985e−09	4.467e+04	8.816e−14
1.105e−01	2.974e−04	8.992e−01	5.297e−02	1.419e+01	1.161e−03	7.816e+02	7.603e−09	4.919e+04	6.718e−14
1.160e−01	3.378e−04	9.459e−01	5.735e−02	1.545e+01	9.153e−04	8.605e+02	5.794e−09	5.417e+04	5.120e−14
1.217e−01	3.838e−04	9.952e−01	6.177e−02	1.684e+01	7.185e−04	9.474e+02	4.417e−09	5.965e+04	3.901e−14
1.277e−01	4.361e−04	1.047e+00	6.616e−02	1.836e+01	5.616e−04	1.043e+03	3.369e−09	6.569e+04	2.973e−14
1.341e−01	4.957e−04	1.103e+00	7.046e−02	2.004e+01	4.371e−04	1.148e+03	2.571e−09	7.233e+04	2.265e−14
1.407e−01	5.634e−04	1.161e+00	7.458e−02	2.189e+01	3.389e−04	1.264e+03	1.963e−09	7.965e+04	1.726e−14
1.476e−01	6.404e−04	1.223e+00	7.844e−02	2.392e+01	2.618e−04	1.392e+03	1.499e−09	8.771e+04	1.315e−14
1.549e−01	7.281e−04	1.289e+00	8.193e−02	2.616e+01	2.014e−04	1.533e+03	1.144e−09	9.658e+04	1.002e−14
1.626e−01	8.278e−04	1.358e+00	8.499e−02	2.862e+01	1.544e−04	1.688e+03	8.738e−10	1.064e+05	7.638e−15
1.707e−01	9.412e−04	1.432e+00	8.748e−02	3.133e+01	1.181e−04	1.858e+03	6.672e−10	1.171e+05	5.820e−15
1.791e−01	1.070e−03	1.511e+00	8.934e−02	3.431e+01	9.005e−05	2.046e+03	5.094e−10	1.290e+05	4.434e−15
1.880e−01	1.217e−03	1.595e+00	9.050e−02	3.759e+01	6.851e−05	2.253e+03	3.891e−10	1.420e+05	3.379e−15
1.973e−01	1.384e−03	1.684e+00	9.087e−02	4.121e+01	5.201e−05	2.481e+03	2.972e−10	1.564e+05	2.575e−15
2.070e−01	1.574e−03	1.780e+00	9.037e−02	4.518e+01	3.941e−05	2.731e+03	2.270e−10	1.722e+05	1.962e−15
2.173e−01	1.789e−03	1.881e+00	8.898e−02	4.957e+01	2.979e−05	3.008e+03	1.734e−10	1.896e+05	1.495e−15
2.280e−01	2.034e−03	1.990e+00	8.671e−02	5.439e+01	2.249e−05	3.312e+03	1.324e−10	2.088e+05	1.139e−15
2.393e−01	2.312e−03	2.107e+00	8.361e−02	5.970e+01	1.695e−05	3.647e+03	1.011e−10
2.512e−01	2.628e−03	2.232e+00	7.975e−02	6.555e+01	1.275e−05	4.015e+03	7.718e−11
2.637e−01	2.987e−03	2.366e+00	7.534e−02	7.199e+01	9.585e−06	4.421e+03	5.892e−11
2.767e−01	3.394e−03	2.511e+00	7.047e−02	7.908e+01	7.196e−06	4.869e+03	4.497e−11
2.905e−01	3.855e−03	2.666e+00	6.520e−02	8.688e+01	5.397e−06	5.361e+03	3.433e−11
3.049e−01	4.377e−03	2.833e+00	5.966e−02	9.548e+01	4.044e−06	5.903e+03	2.620e−11
3.201e−01	4.968e−03	3.014e+00	5.401e−02	1.049e+02	3.027e−06	6.501e+03	1.999e−11
3.360e−01	5.636e−03	3.210e+00	4.839e−02	1.154e+02	2.264e−06	7.158e+03	1.525e−11
3.527e−01	6.390e−03	3.421e+00	4.294e−02	1.268e+02	1.692e−06	7.882e+03	1.164e−11
3.702e−01	7.242e−03	3.650e+00	3.774e−02	1.395e+02	1.264e−06	8.679e+03	8.876e−12
3.887e−01	8.202e−03	3.899e+00	3.283e−02	1.534e+02	9.437e−07	9.558e+03	6.771e−12
4.081e−01	9.284e−03	4.169e+00	2.830e−02	1.687e+02	7.047e−07	1.052e+04	5.164e−12
4.285e−01	1.050e−02	4.463e+00	2.417e−02	1.856e+02	5.263e−07	1.159e+04	3.938e−12
4.499e−01	1.186e−02	4.783e+00	2.048e−02	2.042e+02	3.931e−07	1.276e+04	3.003e−12
4.724e−01	1.339e−02	5.132e+00	1.726e−02	2.247e+02	2.938e−07	1.405e+04	2.290e−12
4.961e−01	1.510e−02	5.513e+00	1.445e−02	2.472e+02	2.198e−07	1.547e+04	1.746e−12
5.210e−01	1.700e−02	5.929e+00	1.203e−02	2.720e+02	1.646e−07	1.704e+04	1.331e−12
5.472e−01	1.911e−02	6.384e+00	9.968e−03	2.993e+02	1.234e−07	1.876e+04	1.015e−12

Note. Differential Intensity units: $(\text{m}^2 \text{ s sr GV})^{-1}$.

(This table is available in machine-readable form.)

Table 8
 $Z = 9$ —Total Fluorine LIS with the Primary Component

E_{kin} GeV/n	Differential Intensity								
1.000e−03	8.088e−03	6.309e−02	2.212e−01	3.981e+00	6.206e−03	2.512e+02	4.803e−08	1.585e+04	4.204e−13
1.101e−03	8.828e−03	6.948e−02	2.336e−01	4.384e+00	4.957e−03	2.766e+02	3.646e−08	1.745e+04	3.204e−13
1.213e−03	9.552e−03	7.651e−02	2.458e−01	4.827e+00	3.947e−03	3.046e+02	2.771e−08	1.922e+04	2.442e−13
1.335e−03	1.034e−02	8.425e−02	2.576e−01	5.315e+00	3.131e−03	3.354e+02	2.108e−08	2.116e+04	1.861e−13
1.470e−03	1.119e−02	9.277e−02	2.689e−01	5.853e+00	2.475e−03	3.693e+02	1.605e−08	2.330e+04	1.418e−13
1.619e−03	1.211e−02	1.022e−01	2.793e−01	6.446e+00	1.948e−03	4.067e+02	1.223e−08	2.566e+04	1.081e−13
1.783e−03	1.311e−02	1.125e−01	2.888e−01	7.098e+00	1.527e−03	4.478e+02	9.325e−09	2.825e+04	8.236e−14
1.963e−03	1.420e−02	1.239e−01	2.971e−01	7.816e+00	1.192e−03	4.931e+02	7.112e−09	3.111e+04	6.276e−14
2.162e−03	1.538e−02	1.364e−01	3.042e−01	8.607e+00	9.272e−04	5.430e+02	5.428e−09	3.426e+04	4.783e−14
2.381e−03	1.667e−02	1.502e−01	3.097e−01	9.478e+00	7.184e−04	5.980e+02	4.144e−09	3.773e+04	3.644e−14
2.622e−03	1.806e−02	1.654e−01	3.136e−01	1.044e+01	5.545e−04	6.585e+02	3.164e−09	4.155e+04	2.777e−14
2.887e−03	1.957e−02	1.822e−01	3.156e−01	1.149e+01	4.264e−04	7.251e+02	2.416e−09	4.575e+04	2.116e−14
3.179e−03	2.121e−02	2.006e−01	3.157e−01	1.266e+01	3.268e−04	7.985e+02	1.845e−09	5.038e+04	1.612e−14
3.501e−03	2.298e−02	2.209e−01	3.137e−01	1.394e+01	2.498e−04	8.793e+02	1.409e−09	5.548e+04	1.229e−14
3.855e−03	2.491e−02	2.432e−01	3.095e−01	1.535e+01	1.904e−04	9.682e+02	1.075e−09	6.109e+04	9.362e−15
4.245e−03	2.700e−02	2.678e−01	3.033e−01	1.690e+01	1.448e−04	1.066e+03	8.214e−10	6.727e+04	7.133e−15
4.675e−03	2.927e−02	2.949e−01	2.949e−01	1.861e+01	1.099e−04	1.174e+03	6.274e−10	7.408e+04	5.435e−15
5.148e−03	3.173e−02	3.248e−01	2.843e−01	2.049e+01	8.327e−05	1.293e+03	4.792e−10	8.157e+04	4.141e−15
5.669e−03	3.439e−02	3.577e−01	2.717e−01	2.257e+01	6.295e−05	1.424e+03	3.660e−10	8.983e+04	3.156e−15
6.242e−03	3.728e−02	3.938e−01	2.573e−01	2.485e+01	4.750e−05	1.568e+03	2.795e−10	9.892e+04	2.404e−15
6.874e−03	4.041e−02	4.337e−01	2.414e−01	2.736e+01	3.579e−05	1.726e+03	2.134e−10
7.569e−03	4.379e−02	4.776e−01	2.244e−01	3.013e+01	2.693e−05	1.901e+03	1.629e−10
8.335e−03	4.745e−02	5.259e−01	2.068e−01	3.318e+01	2.024e−05	2.093e+03	1.244e−10
9.179e−03	5.141e−02	5.791e−01	1.890e−01	3.654e+01	1.520e−05	2.305e+03	9.495e−11
1.011e−02	5.569e−02	6.377e−01	1.711e−01	4.023e+01	1.140e−05	2.539e+03	7.247e−11
1.113e−02	6.030e−02	7.022e−01	1.533e−01	4.431e+01	8.538e−06	2.795e+03	5.530e−11
1.226e−02	6.528e−02	7.733e−01	1.361e−01	4.879e+01	6.391e−06	3.078e+03	4.220e−11
1.350e−02	7.065e−02	8.515e−01	1.198e−01	5.373e+01	4.780e−06	3.390e+03	3.220e−11
1.486e−02	7.642e−02	9.377e−01	1.046e−01	5.916e+01	3.572e−06	3.733e+03	2.456e−11
1.637e−02	8.263e−02	1.033e+00	9.049e−02	6.515e+01	2.668e−06	4.110e+03	1.874e−11
1.802e−02	8.930e−02	1.137e+00	7.763e−02	7.174e+01	1.993e−06	4.526e+03	1.429e−11
1.985e−02	9.646e−02	1.252e+00	6.605e−02	7.900e+01	1.488e−06	4.984e+03	1.090e−11
2.185e−02	1.041e−01	1.379e+00	5.575e−02	8.699e+01	1.111e−06	5.489e+03	8.315e−12
2.406e−02	1.123e−01	1.518e+00	4.675e−02	9.580e+01	8.300e−07	6.044e+03	6.341e−12
2.650e−02	1.210e−01	1.672e+00	3.901e−02	1.055e+02	6.203e−07	6.656e+03	4.835e−12
2.918e−02	1.303e−01	1.841e+00	3.239e−02	1.162e+02	4.640e−07	7.329e+03	3.687e−12
3.213e−02	1.402e−01	2.027e+00	2.676e−02	1.279e+02	3.474e−07	8.071e+03	2.811e−12
3.539e−02	1.505e−01	2.233e+00	2.202e−02	1.409e+02	2.605e−07	8.887e+03	2.143e−12

Note. Differential Intensity units: $(\text{m}^2 \text{ sr GeV/n})^{-1}$.

(This table is available in machine-readable form.)

ORCID iDs

M. J. Boschini  <https://orcid.org/0000-0002-6401-0457>
S. Della Torre  <https://orcid.org/0000-0002-7669-0859>
M. Gervasi  <https://orcid.org/0000-0003-3884-0905>
D. Grandi  <https://orcid.org/0000-0003-1942-8587>
G. Jóhannesson  <https://orcid.org/0000-0003-1458-7036>
G. La Vacca  <https://orcid.org/0000-0002-2168-9447>
N. Masi  <https://orcid.org/0000-0002-3729-7608>
I. V. Moskalenko  <https://orcid.org/0000-0001-6141-458X>
T. A. Porter  <https://orcid.org/0000-0002-2621-4440>
P. G. Rancoita  <https://orcid.org/0000-0002-1990-4283>
D. Rozza  <https://orcid.org/0000-0002-7378-6353>
M. Tacconi  <https://orcid.org/0000-0002-9344-6305>

References

Aguilar, M., Aisa, D., Alpat, B., et al. 2014, *PhRvL*, **113**, 221102
Aguilar, M., Aisa, D., Alpat, B., et al. 2015a, *PhRvL*, **114**, 171103
Aguilar, M., Aisa, D., Alpat, B., et al. 2015b, *PhRvL*, **115**, 211101
Aguilar, M., Ali Cavasonza, L., Alpat, B., et al. 2016a, *PhRvL*, **117**, 091103
Aguilar, M., Ali Cavasonza, L., Alpat, B., et al. 2017, *PhRvL*, **119**, 251101
Aguilar, M., Ali Cavasonza, L., Alpat, B., et al. 2018b, *PhRvL*, **121**, 051103
Aguilar, M., Ali Cavasonza, L., Alpat, B., et al. 2019b, *PhRvL*, **122**, 101101
Aguilar, M., Ali Cavasonza, L., Ambrosi, G., et al. 2016b, *PhRvL*, **117**, 231102
Aguilar, M., Ali Cavasonza, L., Ambrosi, G., et al. 2018a, *PhRvL*, **120**, 021101
Aguilar, M., Ali Cavasonza, L., Ambrosi, G., et al. 2019a, *PhRvL*, **122**, 041102
Aguilar, M., Ali Cavasonza, L., Ambrosi, G., et al. 2020, *PhRvL*, **124**, 211102
Aguilar, M., Ali Cavasonza, L., Ambrosi, G., et al. 2021d, *PhR*, **894**, 1
Aguilar, M., Cavasonza, L. A., Allen, M. S., et al. 2021a, *PhRvL*, **126**, 081102
Aguilar, M., Cavasonza, L. A., Allen, M. S., et al. 2021c, *PhRvL*, **126**, 041104
Aguilar, M., Cavasonza, L. A., Alpat, B., et al. 2021b, *PhRvL*, **127**, 021101
Ahn, H. S., Allison, P., Bagliesi, M. G., et al. 2009, *ApJ*, **707**, 593
Ahn, H. S., Allison, P. S., Bagliesi, M. G., et al. 2008, *Aph*, **30**, 133
Asplund, M., Grevesse, N., Sauval, A. J., & Scott, P. 2009, *ARA&A*, **47**, 481
Barashenkov, V. S., & Polanski, A. 1994, *Electronic Guide for Nuclear Cross Sections*, Tech. Rep. E2-94-417, Comm. JINR, Dubna, <http://cds.cern.ch/record/278901/files/SCAN-9503228.pdf>
Bobchenko, B. M., Buklej, A. E., Vlasov, A. V., et al. 1979, *SvJNP*, **30**, 805
Bobik, P., Boschini, M. J., Della Torre, S., et al. 2016, *JGRA*, **121**, 3920

- Boschini, M. J., Della Torre, S., Gervasi, M., et al. 2017, *ApJ*, **840**, 115
- Boschini, M. J., Della Torre, S., Gervasi, M., et al. 2018a, *ApJ*, **854**, 94
- Boschini, M. J., Della Torre, S., Gervasi, M., et al. 2018b, *ApJ*, **858**, 61
- Boschini, M. J., Della Torre, S., Gervasi, M., et al. 2020a, *ApJS*, **250**, 27
- Boschini, M. J., Della Torre, S., Gervasi, M., et al. 2021, *ApJ*, **913**, 5
- Boschini, M. J., Della Torre, S., Gervasi, M., La Vacca, G., & Rancoita, P. G. 2019, *AdSpR*, **64**, 2459
- Boschini, M. J., Torre, S. D., Gervasi, M., et al. 2020b, *ApJ*, **889**, 167
- Cummings, A. C., Stone, E. C., Heikkila, B. C., et al. 2016, *ApJ*, **831**, 18
- Di Felice, V., Pizzolotto, C., D'Urso, D., et al. 2017, *ICRC (Busan)*, **35**, 1073
- Engelmann, J. J., Ferrando, P., Soutoul, A., et al. 1990, *A&A*, **233**, 96
- Goriely, S., Jorissen, A., & Arnould, M. 1990, in *Nuclear Astrophysics*, 5th Workshop, 60, ed. W. Hillebrandt & E. Müller (Garching: Max-Planck-Institut für Astrophysik), 60
- Grebenyuk, V., Karmanov, D., Kovalev, I., et al. 2019, *AdSpR*, **64**, 2559
- Jóhannesson, G., Ruiz de Austri, R., Vincent, A. C., et al. 2016, *ApJ*, **824**, 16
- Lave, K. A., Wiedenbeck, M. E., Binns, W. R., et al. 2013, *ApJ*, **770**, 117
- Maurin, D., Melot, F., & Taillet, R. 2014, *A&A*, **569**, A32
- Meynet, G., & Arnould, M. 2000, *A&A*, **355**, 176
- Moskalenko, I. V., Vladimirov, A. E., Porter, T. A., & Strong, A. W. 2013, *ICRC (Rio de Janeiro)*, **33**, 0823
- Olive, K. A., & Vangioni, E. 2019, *MNRAS*, **490**, 4307
- Panov, A. D., Adams, J. H., Ahn, H. S., et al. 2009, *BRASP*, **73**, 564
- Prantzos, N., Abia, C., Limongi, M., Chieffi, A., & Cristallo, S. 2018, *MNRAS*, **476**, 3432
- Renda, A., Fenner, Y., Gibson, B. K., et al. 2004, *MNRAS*, **354**, 575
- Ryde, N., Jönsson, H., Mace, G., et al. 2020, *ApJ*, **893**, 37
- Vladimirov, A. E., Jóhannesson, G., Moskalenko, I. V., & Porter, T. A. 2012, *ApJ*, **752**, 68
- Wellisch, H. P., & Axen, D. 1996, *PhRvC*, **54**, 1329